Ocean Sci. Discuss., 12, 1913–1952, 2015
www.ocean-sci-discuss.net/12/1913/2015/
doi:10.5194/osd-12-1913-2015
© Author(s) 2015. CC Attribution 3.0 License.

Ocean Science
Discussions
Open Access

This discussion paper is/has been under review for the journal Ocean Science (OS).
Please refer to the corresponding final paper in OS if available.

A combined quality-control methodology in Ebro Delta (NE Spain) high frequency radar system

P. Lorente[1], S. Piedracoba[2], J. Soto-Navarro[1], and E. Alvarez-Fanjul[1]

[1]Puertos del Estado, Avenida del Partenón 10, 28042, Madrid, Spain
[2]University of Vigo, Marcosende s/n, 36310, Vigo, Pontevedra, Spain

Received: 16 July 2015 – Accepted: 25 July 2015 – Published: 24 August 2015

Correspondence to: P. Lorente (plorente@puertos.es)

Published by Copernicus Publications on behalf of the European Geosciences Union.

Abstract

Ebro River Delta is a relevant marine protected area in the western Mediterranean. In order to promote the conservation of its ecosystem and support operational decision making in this sensitive area, a three site standard-range (13.5 MHz) CODAR SeaSonde High Frequency (HF) radar was deployed in 2013. Since there is a growing demand for reliable HF radar surface current measurements, the main goal of this work is to present a combined quality control methodology. Firstly, one year-long (2014) real-time web monitoring of nonvelocity-based diagnostic parameters is conducted in order to infer both radar site status and HF radar system performance. Signal-to-noise ratio at the monopole exhibited a consistent monthly evolution although some abrupt decreases (below 10 dB), occasionally detected in June for one of the radar sites, impacted negatively on the spatiotemporal coverage of total current vectors. It seemed to be a sporadic episode since radar site overall performance was found to be robust during 2014. Secondly, a validation of HF radar data with independent in situ observations from a moored current meter was attempted for May–October 2014. The accuracy assessment of radial and total vectors revealed a consistently high agreement. The directional accuracy of the HF radar was rated at better than 8°. The correlation coefficient and RMSE values emerged in the ranges 0.58–0.83 and 4.02–18.31 cm s^{-1}, respectively. The analysis of the monthly averaged current maps for 2014 showed that the HF radar properly represented basic oceanographic features previously reported, namely: the predominant southwestward flow, the coastal clockwise eddy confined south of Ebro Delta mouth or the Ebro River impulsive-type freshwater discharge. Future works should include the use of verified HF radar data for the rigorous skill assessment of operational ocean circulation systems currently running in Ebro estuarine region like MyOcean IBI.

OSD
12, 1913–1952, 2015

1 Introduction

The circulation in Ebro continental margin (NE Spain, Fig. 1a) is mainly thermohaline and characterized by a quasi-permanent barotropic shelf-slope jet which flows southwestwards, "the North current", only altered by clockwise inertial oscillations and some short periods of current reversals. This relatively low-intensity current flow ($10\,cm\,s^{-1}$) is in geostrophic balance with the so-called Catalan front, which is a permanent density front associated with strong salinity gradients maintained by the Ebro River runoff (Font et al., 1988a).

The marine circulation near the delta, although dominated by the alongshore large-scale dynamic, presents a complex structure strongly influenced by the topography, the seasonality of the remarkable Ebro River discharges (Font et al., 1988b), the changing wind conditions and the water column thermal stratification (Salat et al., 2002). Nonetheless, the tidal influence in the continental shelf currents field is very weak as expected for a microtidal and low-energy environment (Jimenez et al., 2002).

Since the Ebro River Delta is one of the most relevant marine protected areas in the western Mediterranean in terms of biodiversity, an important monitoring activity is performed to manage this deltaic coastal region and promote the conservation of its ecosystem. In order to support marine domain awareness and operational decision making in this sensitive area, a 13.5 MHz CODAR SeaSonde High Frequency (HF) radar, able to monitor the spatiotemporal evolution of the surface current fields in near real-time, has been deployed (Fig. 1b). This shore-based remote-sensing technology presents a broad range of practical applications, encompassing management (SAR operations, oil spill emergencies), commercial (vessel tracking, ocean energy production) and research (ecology, water quality, fisheries) uses.

As a consequence, there is a growing demand for reliable and accurate HF radar surface current measurements. Since HF radar estimations are subject to many potential uncertainties (namely: radio frequency interferences, ionosphere clutter, antenna pattern distortions or environmental noise – see Kohut and Glenn, 2003), radar status

OSD
12, 1913–1952, 2015

and performance must be routinely examined by means of the development of quality check procedures and the execution of continuous validation works with independent in situ instruments.

The development of quality control (QC) procedures, implemented at various stages of data processing, constitutes an ongoing research area. A dedicated web interface has been developed to operationally monitor in real time the evolution of a variety of nonvelocity-based diagnostic parameters provided by the manufacturer (CODAR Ocean Sensors – COS) and listed in Table 1. Such parameters are used as indicators of HF radar system integrity and health (Roarty et al., 2012; Emery and Washburn, 2007) since anomalous values, inconsistencies or sharp fluctuations might be related to quality degradation, potential malfunctions, or even failure problems, triggering alerts for troubleshooting.

Many efforts have been recently devoted to identify occasional non-realistic radar current vectors, generally detected at the outer edges of the radar domain and flagged in accordance with a pre-defined protocol. An individual QC index, based on an integer number derived from a battery of tests, should be assigned for each and every single radar grid-cell to indicate the quality level of each measured value (Gomez et al., 2015).

The artefacts (defined as spikes, spurious values or corrupted data) can be subsequently eliminated from the data stream in real time (Cosoli et al., 2012b) or offline (Liu et al, 2014). Other approaches are focused, in addition, on replacing noisy values with more reliable estimates (Wyatt et al., 2015) by using open-boundary model analysis (Kaplan and Lekien, 2007) or statistical mapping (Barrick et al., 2012). However, the main drawback lies with the potential removal of accurate data when the discriminating algorithm is based on tight thresholds. Some fine-tuning, based on the specific local conditions of the system, is thus required to have the right trade-off between confirmed outlier identification and false alarm rate, maximizing the benefit of the applications of these methods (Gomez et al., 2014).

Whereas some quality indexes are assigned according to velocity-based QC schemes, other approaches intend to use nonvelocity-based metrics related to the

OSD
12, 1913–1952, 2015

characteristics of the received signal in order to implement advanced quality controls and reduce the systematic errors in radar current estimates (Kirincich et al., 2002). One of the radial metrics that offers the most potential benefits as reliability indicator is the Signal-to-Noise Ratio at the monopole (SNR3), since it has been previously proved to be a valid proxy for radar data quality (Cosoli et al., 2012b). Complementarily, a big jump in the average state over time in antenna parameters (e.g. amplitude corrections for loops 1 and 2 to the monopole, AMP1 and AMP2, respectively) may indicate an antenna problem and should be investigated (COS, 2005).

In this context, a number of previous works have focused on defining optimum threshold levels since there is still no worldwide consensus (Kirincich et al., 2012). Atwater and Heron (2011) showed that a simple thresholding of SNR3 is a good starting point, although a 20 dB limit constitutes a too severe QC criterion with a resulting detrimental impact on coverage area. Values of SNR3 below 10 dB have been proved to be closely linked to a significant decrease of the Multiple Signal Characterization (MUSIC) direction-finding algorithm skill (De Paolo and Terril, 2007). As MUSIC is employed to resolve ocean surface current structure (Schmidt, 1986), limitations in its performance are related to potentially suspect velocity outputs. Furthermore, different combinations of dynamic thresholds cutoffs have been analyzed to quantify the potential for error reduction (De Paolo et al., 2015). Since the question still remains open, further researches are currently underway to shed light on it.

In addition, the credibility of HF radar data has been previously tested in extensive validation studies, including direct comparisons of HF radar-derived surface currents with moored ADCP's, point-wise current meters or drifters (Graber et al., 1997; Kaplan et al., 2005; Cosoli et al., 2010). Accordingly, a number of validation works with in situ current sensors have been performed with the HF coastal radar network operated by Puertos del Estado (Fig. 1a) – PdE hereinafter – in order to quantify and lower uncertainties in radar estimations at both the radial and total vector level (Alfonso et al., 2006; Lorente et al., 2014, 2015a, b).

OSD
12, 1913–1952, 2015

Correlation coefficients (CORR) and root mean squared errors (RMSE) have been previously found to be in the ranges 0.32–0.92 and 6–30 $cm\,s^{-1}$, respectively (Kohut and Glenn, 2003; Paduan et al., 2006; Chapman and Graber, 1997). Relative HF radar velocity errors can vary dramatically with the radar transmission frequency, sensor type and location within the sampled domain, as well as the data processing scheme used (Rypina et al., 2014; Kirincich et al., 2012). In this frame, the instrumental noise and sub-grid scale current variability have been reported to yield noise levels of 4–6 $cm\,s^{-1}$ (Emery et al., 2004; Ohlmann et al., 2007; De Paolo et al., 2015).

The main goal of this work is to present a combined QC methodology for the specific case of Ebro HF radar (although easily expandable to the rest of PdE radar systems): one year-long (2014) real-time web monitoring of diagnostic parameters and regular offline validation of HF radar-derived current data with in situ observations from a point-wise current meter, installed in a buoy moored within the radar domain (B1, Fig. 1b). This integrated approach is applied during 2014 in order to infer both radar site status and HF radar system overall performance and also to provide upper bounds on both radial and total radar current measurement accuracy (Lorente et al., 2015c). Once HF radar data quality is estimated, Ebro Delta HF radar capabilities in reproducing well-known circulation features are investigated through the exploration of monthly averaged flow patterns and dominant modes of variability both in time and space (Cosoli et al., 2012a, 2013; Kovacevik et al., 2004).

This paper is organized as follows: Sects. 2 and 3 outline the specific instrumentation and methods used in this study, respectively, followed in Sect. 4 by a detailed discussion of the results. Finally, main conclusions are summarized in Sect. 5.

OSD
12, 1913–1952, 2015

2 Instrumentation

2.1 HF radar

A CODAR SeaSonde standard-range HF radar system was deployed at Ebro Delta in December 2013 within the frame of RIADE (Redes de Indicadores Ambientales del Delta del Ebro) project. The HF radar network consists of an array of three remote shore-based sites: Salou, Vinaroz and Alfacada. They will hereafter be referred to by their four letter site codes: SALO, VINA and ALFA, respectively (Fig. 1b).

The HF radar technology, founded on principle of Bragg scattering of the electromagnetic radiation over a rough sea (Crombie, 1955), infers the radial current component from the Doppler-shift of radio waves back-scattered by surface gravity waves of half their electromagnetic wavelength. Each single radar site is configured to estimate radial currents moving toward or away from the receive antenna. Since the speed of the wave is easily derived from linear wave theory, the velocity of the underlying ocean surface currents can be computed by subtraction. The distance to the backscattered signal is determined by range-gating the returns and the angle of origin is inferred, in the case of CODAR SeaSonde radars, by a direction-finding process (Barrick and Lipa, 1997) using three collocated receive antennas (two orthogonal closed loops and a single monopole) and the MUSIC algorithm (Schmidt, 1986).

Each site is operating at a nominal frequency of 13.5 MHz with a 90 KHz bandwidth, providing hourly radial measurements with a cut-off filter of 100 $\mathrm{cm\,s^{-1}}$ and representative of current velocities in the upper first meter of the water column. Only calibrated (measured) antenna beam patterns (hereinafter APM) were employed by the manufacturer supplied software to process radial data used in the present study, with the aim of maximizing HF radar usefulness for operational applications (Lipa et al., 2006; Kohut and Glenn, 2003). In regions of overlapping coverage from two or more sites, radial current measurements are geometrically combined using a least-square fit technique (Barrick and Lipa, 1986) with the averaging radius set to 6 km in order to estimate hourly averaged total current vectors on a predefined Cartesian regular grid with 3 km × 3 km

OSD
12, 1913–1952, 2015

horizontal resolution. The maximum horizontal range is set to 80 km and the angular resolution is 5°.

HF radar-derived data used in this study have been collected from 1 January to 31 December 2014. During this period the three sites were simultaneously operational and radar coverage was as its maximum extent. Temporal data coverage was quantified by computing the percent of total possible vector returns at each radar grid point (Fig. 1b). Percent coverage decreases rapidly near the outer edges of the domain where error levels are higher due to poor intersecting beam geometry (Chapman and Graber, 1997) and quantified by larger Geometric Dilution of Precision (GDOP, Chapman et al, 1997). GDOP is an unit-less coefficient of uncertainty that characterizes how radar geometry may impact on measurements accuracy and position determination errors, owing to the angle at which the radials intersect and also to uncertainties in the radial vectors geometrically combined (Levanon, 2000; Trujillo et al., 2004).

With the aim of screening out radar grid points where data are less reliable, a threshold on percent coverage has been imposed. Only time series of zonal and meridional surface currents at grid points with percent coverage greater than 50 % over the 2014 annual record have been considered in this study. The selected coverage area present associated GDOP values of 1.5 or less.

2.2 Buoy B1

The domain of Ebro Delta HF radar array includes an ocean Seawatch buoy deployed since August 2004 in the eastern waters of the Iberian Peninsula: Tarragona buoy (40.68° N, 1.47° E, 688 m depth), hereafter referred to as B1 (Fig. 1b). This buoy is equipped with an acoustic point-wise current meter manufactured by Falmouth Scientific Inc., providing quality-controlled hourly averaged current velocity vectors at a nominal depth of three meters. It should be noted that current and wind records from B1 are only available from 1 May to 31 October 2014. B1 suffered from brief communication outages during this period and subsequent short gaps (2–3 h) in data time series have been linearly interpolated.

OSD
12, 1913–1952, 2015

3 Methods

3.1 Online Quality Control of HF radar measurements

In order to ensure the reliability of the HF radar products delivered, maintenance and Quality Control (QC) procedures must be performed at various stages on the data generation pipeline. The manufacturer software package integrates a set of QC routines and thresholding techniques in the data processing chain (e.g., limits for maximum vector magnitude and maximum GDOP).

This section presents a simplistic approach based on additional data quality checks at the post-processing stage and devoted to examine a variety of nonvelocity-based indicators (Table 1). Such indicators include hardware, antenna, radial and total parameters, employed here as diagnostic tools for evaluating HF radar integrity and health (Roarty et al., 2012; Emery and Washburn, 2007). A dedicated online website has been developed to operationally monitor radar site status since anomalous values, inconsistencies or sharp fluctuations in the indicators might be related to potential malfunctions. This automated quality control web tool runs in background with a cron job, being updated on an hourly basis.

One year-long (2014) real-time monitoring has been performed in order to inspect the temporal evolution of the aforementioned parameters, obtain estimates of their standard ranges and evaluate Ebro Delta radar site performance according to them (Lorente et al., 2015a). Abrupt or gradual degradation and failure problems can be easily detected, triggering alerts for troubleshooting when defined thresholds (initially set to two standard deviations above/below the mean) are persistently exceeded. Particular emphasis has been devoted to SNR3 as it has been previously analyzed as valid proxy for radar data quality (Cosoli et al., 2012b).

Finally, automated quality checks have been implemented at the second level within the hierarchy defined for QC procedures, referred to total vectors. Temporal and spatial coverage of Ebro Delta radar system are separately analyzed on a monthly basis and later confronted to each other to check if HF radar systems operate within tolerance

OSD
12, 1913–1952, 2015

ranges, fulfilling the recommended level of data provision: 80 % of the spatial region over the 80 % of the time (Roarty et al., 2012).

3.2 HF radar validation

HF radar measurements are subject to many potential errors as a consequence of inherent problems of radar technology, such as power-line disturbances, sea clutter, ship and ionosphere echoes or weather-depended and interference-sensitive coverage (Graber et al., 1997). Direct comparisons against other in situ sensors (ADCP's, point-wise current meters – PCM hereinafter –, drifters or similar) permit an independent assessment of HF radar performance together with a quantitative estimation of uncertainties in radar current measurements.

Since the Ebro Delta HF radar footprint overlooks of a moored PCM within its spatial coverage, an accuracy assessment of radar surface currents is performed for a 6 month period May–October 2014 of concurrent radar-PCM measurements. The present section builds on previous investigations devoted to the determination of measurements errors, the evaluation of direction-finding capabilities and the angular distribution of radial velocity uncertainties (Emery et al., 2004; Paduan et al., 2006; Cosoli et al., 2010; De Paolo and Terrill, 2007).

To this aim, the radar radial arc geographically closest to B1 buoy location has been selected for each HF radar site and radial current vectors estimated at each arc point have been compared with the radial projection of PCM velocities. The B1-HF radar comparative analysis allows the computation of statistical parameters (e.g., CORR and RMSE) as a function of the angle comprised between B1 and the arc grid point position. In absence of direction-finding errors (DF), maximum CORR and minimum RMSE values should be found over the arc point closest to B1 location. In presence of DF, the bearing offset is thus expressed as the angular difference between the arc point with maximum correlation and the buoy location.

Radial current time series have been filtered to remove all tidal, diurnal and inertial fluctuations (the inertial period is 18.4 h at B1 location latitude) from the velocity data.

OSD
12, 1913–1952, 2015

Filtered time series, obtained after applying a 10th order digital low-pass Butterworth filter with a cut-off period of 30 h (Emery and Thomson, 2001), have been compared to evaluate the discrepancies in subinertial currents.

Complementarily, HF radar total vector hourly estimations at the grid point closest to B1 location (HFR1, 1.48° E 40.69° N, Fig. 1b) have been compared with PCM velocities to provide upper bounds on the radar current measurement accuracy. Comparisons have been undertaken using zonal (U) and meridional (V) components in order to evaluate the agreement between both instruments by means of the computation of a set of statistical metrics – RMSE, scalar and complex correlations and best linear fit of scatter plots. Monthly results have been summarized with Taylor diagrams (Taylor, 2001), which provide a concise statistical summary of the agreement between both datasets.

Finally, rotatory spectral analyses (Gonella, 1972) have been performed for HF radar-derived total vectors at HFR1 location and for current data from B1 in order to identify the dominant modes of temporal variability. To ensure the continuity of the data record, small gaps detected (not larger than 6 h) in time series have been linearly interpolated. Spectra have been calculated by dividing time series into successive six day segments, with a 50 % overlap and a Hanning window (Emery and Thompson, 2001), and subsequently averaged to provide some smoothing.

3.3 Characterization of the surface circulation field

The ability of HF radar to reproduce well-known circulation features in Ebro Delta area has been investigated through the exploration of mean flow patterns and dominant modes of surface current variability. To this purpose, maps of the Eulerian mean current field have been constructed at monthly time scale from the raw radar time series on a subsampled grid. As previously mentioned, only radar grid points satisfying a minimum data return of 50 % over the monthly record have been considered. Due to this constraint, the study area was not uniformly covered.

Additionally, a complex Empirical Orthogonal Function (EOF) decomposition (Kundu and Allen, 1976) has been used to infer the driving forces and spatiotemporal scales

OSD
12, 1913–1952, 2015

behind the variability of sea surface currents (Kaihatu et al., 1998). This method, which reduces the components of the vector field to a complex scalar, has become widespread in order to extract the dominant modes of variability. The representative spatial patterns (or EOF modes) and their corresponding temporal coefficients (which describe the evolution of the modes) are determined by using the singular value decomposition of the covariance matrix. Each statistically significant EOF mode explains a limited portion of the total surface current variance.

EOF analysis has been applied to radar current velocity dataset using the raw, unfiltered hourly time series for the entire year 2014. Main spatial modes obtained for HF radar have been interpreted in terms of physical processes related to the detected spatially coherent structures. Since the modes are uncorrelated, observed current fields can be reproduced by using the first few modes which contain a significant portion of the total variance.

4 Results and discussion

4.1 Annual quality control

This analysis aims to quantify the consistency of nonvelocity-based diagnostic parameters over the nearly continuous 1 year time series, as indicators of HF radar regular status in terms of robustness and stable performance.

Since SNR3 has been previously analyzed as valid proxy for radar data quality (Cosoli et al., 2012b), its evolution has been routinely monitored during 2014. Box plots of SNR3 for each radar site (Fig. 2a–c) exhibit a consistent monthly evolution, with a median (central mark) above 40 dB. However, a number of sharp decreases can be occasionally observed in VINA site for the month of June (Fig. 2c), exceeding the previously reported threshold of 10 dB (De Paolo and Terril, 2007).

The annual time serie of hourly SNR3 values for VINA site (Fig. 2d) reveals that the thresholds proposed in the present work (two standard deviations above/below the

OSD
12, 1913–1952, 2015

mean, represented by bold blue dotted lines) were abruptly exceeded several times in June. SNR3 reached extremely low values, leading to a drastic reduction in the radar spatial coverage presumably related to limitations in the MUSIC algorithm. Consequently, the number of radial vectors (NRV) provided by VINA lowered significantly in June (Fig. 2e). Leaving aside the regular high frequency fluctuations due to the day/night cycle, NRV was several times below 500 and even equal to zero, indicating a poorer than expected performance of VINA site during this month. Nonetheless, it appears to be a sporadic episode, maybe related to radio-wave interferences, since VINA presented a stable performance during the second semester of 2014.

The quality checks implemented at total vectors level allow an overall evaluation of Ebro Delta HF radar system performance on a monthly basis (Fig. 3). A comparative analysis for February and June confirms the degraded performance during the latter. Data availability generally exceeded 80 % in time over the majority of the radar footprint in February, with an abrupt decrease at the periphery of the radar range (Fig. 3a). By contrast, it only outreached the 50 % in June, with a smoother transition at the outer edges of the domain (Fig. 3b). The evolution of the spatial coverage was rather consistent in February, with sporadic decreases below 50 % (Fig. 3c). On the contrary, an irregular performance is detected in June as a consequence of both ALFA site outage (1–8 June) and VINA irregular behavior (Fig. 3d). The first factor yielded a dramatic and persistent drop in the areal coverage, lower than 20 % most of the time. The second led to a significant, albeit occasional, reduction in the radar spatial domain (below 50 %), which can be observed from 8 to 30 June 2014.

Finally, the temporal and spatial coverage have been confronted to each other (Fig. 3e and f). Ebro Delta radar system was closer to fulfill the required 80–80 % level of data provision in February (Roarty et al., 2012), with a 64 % of the areal domain (referred to its maximum extent) available the 80 % of the time. By contrast, the radar system barely reached the 35 % of spatial coverage for the 80 % of the time in June. Despite this occasional degradation, radar sites overall performance and their day-to-day operation have been found to be robust and within tolerance ranges, with sporadic

OSD
12, 1913–1952, 2015

interruptions (presumably attributable to power outages) that introduced short-duration gaps in time and space.

It is noteworthy that the described methodology, at this preliminary development stage, is not able to remove suspicious values (outliers, spikes or spurious values) from the data stream in real time like Cosoli et al. (2012b) but only to detect anomalies and categorize them in order to create a historic radial database similar to Roarty et al. (2012) for a later offline reprocessing of total vector maps when one (or more) radar site(s) is (are) considered to be working abnormally. In this context, the hourly radial vectors provided by VINA site in June that did not satisfy the proposed QC control have been discarded from the analyses performed in the next sections and the associated total vector maps have been accordingly reprocessed offline. Future efforts should be devoted to improve radial data quality in real-time prior to the vector combination process and also to assign quality descriptor flags for each grid point data in total current fields.

4.2 Buoy-radar comparison results

In order to assess the reliability of radar surface currents, an error analysis is first performed on the radial velocities from individual radar sites for the 6 month radar-buoy common period (Cosoli et al., 2012a). The evaluation of direction-finding capabilities revealed the existence of small bearing errors (hereafter $\Delta\alpha$) in radar radial estimations, ranging between 2–8° (Fig. 4) and in accordance with the typical values previously reported (Emery et al., 2004; Paduan et al., 2006).

Comparison of unfiltered hourly radial currents estimated by B1 and SALO site (Fig. 4b) shows maximum CORR in a grid point (denoted by vertical solid red line) angularly close to B1 location (vertical dotted black line): 0.79, with associated RMSE of 10.95 $\mathrm{cm\,s^{-1}}$ and $\Delta\alpha$ of 3.74° in the counter-clockwise direction. VINA site (Fig. 4c) presents a lower bearing offset ($\Delta\alpha = 1.82°$) but also lower (higher) CORR (RMSE) value of 0.58 (13.31 $\mathrm{cm\,s^{-1}}$). It is worth mentioning that minimum RMSE values are also placed on the vicinity of the correlation peaks. The VINA site exhibits the largest

OSD
12, 1913–1952, 2015

pointing error ($\Delta\alpha = 7.82^{\circ}$) and the poorest agreement with moored radial estimations as CORR is 0.58 and RMSE is fairly above 18 cm s^{-1} (Fig. 4d).

Hourly time series of low-pass filtered radial currents measured by B1 and those estimated in the closest range arc point ("best match-angle") by each HF radar site are presented in Fig. 5. Metrics derived from the accuracy assessment highlight the consistently high agreement between SALO radar site and B1 estimations, with a CORR and RMSE values of 0.80 and 5.58 cm s^{-1}, respectively (Fig. 5a). Results derived from the best linear fit reveal a slope close to 1 and an intercept up to −0.82 cm s^{-1}. The concordance between ALFA site and B1 is moderately good, with acceptable pairs of values CORR-RMSE and slope-intercept: 0.63–6.91 and 0.73–1.92 cm s^{-1}, respectively (Fig. 5b). VINA site data show lower agreement with in situ measurements (Fig. 5c) as reflected by a lower (higher) CORR (RMSE) value of 0.56 (7.76 cm s^{-1}). This might be partially attributable to the long site-buoy distance (i.e., the radar signal is weaker) and to the limited radar data availability due to day/night coverage fluctuations (i.e., the data return is more than three times lower, with only 986 hourly observations available).

Ancillary validation works with radial measurements like internal self-consistency checks have not been performed due to Ebro Delta radar sites' geometry. Radar-to-radar comparisons along the overwater baselines (Paduan et al., 2006; Yoshikawa et al., 2006; Atwater and Heron, 2010), although valuable to explore quantitatively intrinsic uncertainties in radial velocities, are not feasible since they are positioned over land or near the coastline.

Statistical metrics derived from filtered hourly time series comparison of zonal (U) and meridional (V) components of total vectors estimated by B1 and HFR1 for the 6 month period are presented in Fig. 6. Results reveal a good agreement for both components (CORR above 0.74), in accordance with results reported in the literature (Cosoli et al., 2010; Kaplan et al., 2005). RMSE is significantly higher for the zonal component than the meridional: 12.69 vs. 4.02 cm s^{-1} (Fig. 6a and b). The disparity of uncertainty levels between the east and north component vectors comes for the geometry of the radar vector combination and the prevalent south-southwestward cur-

OSD
12, 1913–1952, 2015

rent flow. This presumably might lead to less (more) precise radial vectors provided by ALFA (SALO) radar site since radial measurements are proved to be more accurate when the dominant current flow moves in the same direction (Robinson et al., 2011). Since ALFA (SALO) site contributed mainly to the HF radar zonal (meridional) current assessment in B1 nearby region, a strong relationship between radial and total vector uncertainties has been evidenced.

The scatter plots (not shown) and the associated best linear fits show that HF radar slightly underestimates total current velocities registered by B1 since the slopes are below 1: 0.71 and 0.67 for U and V components, respectively. The time-averaged complex correlation coefficient between B1 and HFR1 currents at zero lag is 0.77. The related phase is 8.65°, indicating that the former are, on average, slightly right shifted since the veering angle gives the average counter-clockwise turning of the second vector with respect to the first vector (Kundu, 1976).

The monthly mean current values were computed to characterize the main features of the flow in this region. The descriptive statistics reveal predominant negative values for the zonal speed (Fig. 6c) and a quasi-permanent average flow in the N–S direction (Fig. 6d). There is no evidence of a seasonal signal in both zonal and meridional velocity components of radar and B1 surface currents. Therefore, both instruments exhibit similar monthly mean values and variability, capturing the well-known southwestward thermohaline flow and identifying episodic but intense current reversals, as those observed by mid-September (Fig. 6a and b).

The monthly comparison of total vectors, performed on the unfiltered time series, provide a variety of metrics that are concisely summarized in a Taylor diagram (Taylor, 2001), shown in Fig. 7. The diagram compares both data sets by combining information about their relative standard deviations, centered RMSE and CORR, synthetizing the statistical information of how closely the radar measurements at HFR1 grid point match with B1 velocities. As it can be seen, the cluster of points that show best agreement (i.e., are closest to their corresponding reference point, labeled with blue squares) are those corresponding to the period May–September (red squares, sequentially num-

OSD
12, 1913–1952, 2015

bered 1–5). The reported correlation coefficient, standard deviation and RMSE values emerge in the ranges of 0.72–0.83, 10.96–14.18 and 7.48–8.75 cm s^{-1}, respectively, for both zonal and meridional velocity components (Fig. 7a and b). However, HF radar is less accurate by the last month of the analyzed period, since metrics computed for October (red square 6) reflect lower (higher) CORR (RMSE) values: 0.50–0.58 (10.92–11.03).

Instrument-to-instrument comparisons present intrinsic limitations since both devices operate differently and at distinct nominal depths. A fraction of observed radar-B1 differences can thus be explained in terms of different sampling strategies on disparate time and space scales (Ohlmann et al., 2007). In this context, many of the uncertainties associated with HF radar technology are geometric in nature. Apart from the instrumental noise, other sources of potential errors in vector currents might be the sub-grid horizontal shear, the geophysical variability within the water column (Graber et al, 1997) and some specific processes, namely, the Stokes drift, the Ekman drift and baroclinity (Paduan et al., 2006).

Spectral analyses have been computed for a 6 month period May–October 2014 (warm stratified season) to examine power spectral discrepancies in the frequency domain between both instruments. B1 and HFR1 current time series present qualitatively similar characteristics, capturing properly the dominant features within the diurnal and inertial bands, related to significantly prevalent clockwise (CW) rotatory motions (solid lines, Fig. 8). Relevant polarized peaks are evident for both datasets, although their amplitudes are slightly larger for radar currents (solid red line). The inertial peak is the most pronounced, pointing out the adjustment of the stratified fluid to the wind driven currents and, subsequently, the importance of local wind as forcing mechanism (addressed in Sect. 4.3.2). Offshore oscillations in this frequency band are a common feature in ocean circulation and their presence in the study area has been previously documented (Font et al., 1990). By contrast, the counter-clockwise component (CCW, dotted lines) is much less energetic (especially in the case of B1 current estimations) and is where the main radar-B1 differences in variance distribution can be found. Fi-

OSD
12, 1913–1952, 2015

nally, a drop of energy and later flattening about 2 cpd are common for the CW components of both B1 and radar spectra.

4.3 Dominant features of the surface flow

4.3.1 Monthly averaged current patterns

The sequence of monthly averaged current maps in Fig. 9 shows that some of the main circulation features in Ebro Delta remain rather invariant throughout most part of the year, like the southwestward slope jet, associated with the highest velocities detected (above 30 cm s^{-1}). The current speed diminishes toward coastal areas, except in the vicinity of ALFA radar site, where the signal of Ebro River impulsive-type freshwater outflow is clearly evidenced during winter and spring (Fig. 9a, b and f). As a consequence of the remarkable seasonal variability of Ebro discharge rates, the estuarine plume loses intensity during the warm season (Fig. 9c), becoming barely noticeable in late summer and early autumn (Fig. 9d and e), until the beginning of the following hydrological cycle (Fig. 9f).

It is noteworthy the weakening of the southwestward slope jet during the central part of the year, in agreement with reported short periods of current reversals (Font et al., 1990). The jet is intensified in October as a result of the increase of the mesoscale activity (Font et al., 1995), reaching ultimately a peak strength in December. By the end of 2014, the monthly spatial patterns become rather uniform, revealing the acceleration of the jet (with a spatial propagation of maximum velocities, exceeding 40 cm s^{-1}) on the eastern region of the radar domain and also the presence of two small-scale coastal meanders (Fig. 9e and f).

A coastal anticyclonic eddy can also be observed in radar data, confined south of Ebro Delta mouth (Fig. 9a–c). This well-documented hydrodynamic feature is due to the interaction of the buoyancy-driven flow with the topography, reinforcing the shelf/slope front that drives the general circulation to the south-southwest (Font et al., 1990; Salat et al., 2002). In addition, persistent and high-intensity NW wind jets, dominant dur-

OSD
12, 1913–1952, 2015

ing the October–May cold season and channeled by the narrow Ebro Valley, introduce negative vorticity in the flow south of the Ebro Delta and reinforce the long-time preservation of this small-scale eddy (Garcia and Ballester, 1984; Espino et al., 1998). Notwithstanding, this coastal clockwise rotation is eventually absent from September (not shown) to December monthly averaged current maps.

During the transition month of August, a large anticyclonic recirculation cell is evidenced, detached from the shore and located on the center of radar domain (Fig. 9d). This current pattern is dominated by the interaction of the cross-shelf flow on the southern inner shelf with topographic obstacles, giving rise to a shift to the right of the coastal flow. The subsequent northeastward reversal of the inshore flow is scarcely influenced by Ebro River freshwater discharge as it reaches the lowest value at this stage of the year.

4.3.2 Empirical orthogonal function (EOF) analysis

The mean and EOFs of hourly surface currents have been calculated for a 1 year time period (2014) when the three radar sites were simultaneously operational (Fig. 10). The long-term mean flow (Fig. 10a) captures the main circulation features previously reported about "the North Current", characterized by a quasi-permanent shelf-slope jet oriented southwestward and a remarkable Ebro River impulsive-type freshwater discharge (located in front of ALFA site). The buoyancy input introduced by large estuarine outflows, together with topographic effects, lead to the development of the aforementioned anticyclonic coastal eddy on the southern side of the delta.

Since the EOF analysis has been performed on the unfiltered data set containing significant high-frequency spatiotemporal variability, the first three EOFs cumulatively account only for the 46.1 % of the total variance (26.1, 15.3 and 4.7 %, respectively). Higher order modes will not be further addressed here as they represent a combination of unresolved high-frequency motions or noise (Cosoli et al., 2012a).

The first dominant EOF mode (Fig. 10b) represents a spatially uniform pattern, rather similar to the annual averaged current map, with an alongshore shelf-slope jet flowing

OSD
12, 1913–1952, 2015

mainly southwestward, basically capturing the thermohaline Catalan front. The second EOF (Fig. 10c) shows a homogeneous spatial structure, perpendicular to the first mode, with a well-defined offshore-directed flow presumably driven by persistent and intense (up to 100 km h^{-1}) northwesterly winds (called "mistral winds") channeled by the narrow Ebro Valley (Font, 1990). The spatial pattern of EOF3 (Fig. 10d) adds some complexity to the basic uniform flows represented by the first two modes, since it introduces curvature to the current field by means of a large, albeit weak, anticyclonic recirculation cell (flow divergence) in the central (southern) region of the radar domain.

Temporal variation in the strength of these three EOF modes is represented by their corresponding time coefficients, shown in Fig. 11. EOF1 is predominantly positive except during the summertime, when the quasi-permanent flow to the SW is altered by clockwise inertial oscillations (positive EOF3) and some periods of current reversals, with maximum occurrence during the stratified warm season (Font et al., 1990). Nevertheless, EOF1 becomes again strongly positive during the autumn, reaching a peak by mid-December, in clear agreement with the strengthened shelf-slope jet flowing southwestwards shown in Fig. 9f. The temporal structure of EOF2 reveals a principal offshore-directed flow through January–May period and also in late December, as response to both mistral energetic wind, dominant during the cold season (October–May), and Ebro River high discharge rates. Lastly, EOF3 adds clockwise curvature most part of the year (February–September and November). The evident enhancement of the anticyclonic gyre in August (positive EOF3), combined with the onshore-directed flow (negative EOF2) and the reversal of the main current flow (negative EOF1) during that time period, gave rise to a complex circulation scheme, rather similar to the monthly averaged pattern represented in Fig. 9d.

5 Summary and concluding remarks

Since radar measurements are prone to errors, the acquisition of high-quality surface current data remains as a priority for HF radar operators and the research community.

OSD
12, 1913–1952, 2015

In the present work, a combined quality control (QC) methodology has been presented for a three site standard-range (13.5 MHz) CODAR SeaSonde HF radar network deployed at Ebro Delta (NE Spain). This integrated approach consists of one year-long (2014) real-time web monitoring of nonvelocity-based diagnostic parameters, coordinated with a regular offline validation of HF radar data with independent in situ observations.

Signal-to-noise ratio at the monopole (SNR3) has been routinely monitored as it has been proved to be a valid indicator of both radar site status and HF radar system overall performance. Box plots of SNR3 for each radar site exhibited a consistent monthly evolution for 2014, although a number of sharp decreases have been occasionally detected in June for VINA site, exceeding the previously reported threshold of 10 dB and the limits of two standard deviations proposed in the present work. The abrupt drop in SNR3 values of VINA impacted negatively on the number of radials provided and, subsequently, in the spatiotemporal coverage of total current vectors during June. Notwithstanding, it seems to be a sporadic episode since the overall performance of radar sites and their day-to-day operation have been found to be robust and within tolerance ranges. One year of continuous operation revealed three sites up and operational in excess of 95 % of the time, with occasional interruptions that introduced short-duration gaps in time and space.

Complementarily, a regular offline validation of HF radar-derived current data with independent in situ instruments is essential in order to provide lower bounds on radar current measurement uncertainties. To this aim, an accuracy assessment of Ebro Delta radar system estimations was attempted by means of a comparison with measurements from a point-wise current meter installed in B1 buoy, moored within the radar footprint, for a 6 month period May–October 2014 when they were operating simultaneously.

The comparison was carried out at both the radial and total vector levels. Regarding the former, the directional accuracy of the HF radar was rated at better than 8°, suggesting that radar sites were functioning properly and that their APMs were cor-

OSD
12, 1913–1952, 2015

rectly performed and integrated in the data processing. The correlation coefficient and RMSE values emerged in the ranges 0.58–0.79 and 10.95–18.31 cm s^{-1}, respectively. Concerning the total velocity vectors, hourly current time series were compared for a single grid-point in the HF radar domain corresponding to B1 location. The zonal and meridional components of radar surface currents tracked B1 subsurface currents fairly well. The correlation coefficient and RMSE values lied in the ranges 0.72–0.83 and 4.02–12.69 cm s^{-1}, respectively, consistent with previously reported values (Kaplan et al., 2005; Cosoli et al., 2010), indicating that both instruments were indeed producing valid measurements of the current field during the concurrent period of records. Both systems described a predominant southwestward flow, with similar monthly mean values and variability. Therefore, Ebro Delta HF radar proved to have very satisfactory level of accuracy. The overall stable and accurate performance for 2014, derived from the combined QC-validation approach, provides ground truth to examine future radar performances.

The analysis of the monthly averaged spatial patterns of the velocity field shows that the HF radar properly represents basic oceanographic features and recurrent circulation patterns previously observed in the study area, namely: the predominant southwestward flow, the coastal clockwise eddy confined south of Ebro Delta mouth or the Ebro River impulsive-type freshwater discharge. It is also noteworthy that this study has been performed in a low-energy shelf where the surface currents are generally weaker than most of those referenced herein (Lorente et al., 2014).

The EOF analysis confirmed that the surface current field evolved in space and time according to three dominant modes of variability, which account for the 46.1 % of the variance. A year-round overall prevailing shelf-slope jet flowing southwestward is described by the first mode (21.6 % of the variance), with the other two modes superimposed onto it, accounting for the 15.3 and 4.7 % of the variance, respectively. The second mode captures the cross-shelf circulation induced by intense and persistent northwesterly winds while the third introduces complexity to the rather uniform pattern

OSD
12, 1913–1952, 2015

described by the first two modes by adding divergence and vorticity to the surface current field.

Regarding Ebro Delta study area, active and planned efforts are devoted to an extensive description of a variety of marine processes impacting on the evolution and reshape of the nearshore deltaic area: the wave action eroding exposed wetlands, the sediment transport, the freshwater discharges and buoyancy fluxes (which further complicate water motions in the Ebro Estuary) and ultimately the major influence of local wind forcing.

With respect to HF radar, it has been steadily gaining recognition as an efficient land-based remote sensing instrument for mapping surface currents at high spatial and temporal resolutions in near real time. This technology has become a core operational component of integrated multi-platform ocean observing systems thanks to its ability for long-term coastal environmental monitoring of the spatially evolving surface current field, providing hence a dynamical framework for other observational networks (Shay et al., 2002).

Additional development efforts should address the rigorous skill assessment of operational ocean circulation systems currently running in Ebro estuarine region like MyOcean IBI (Sotillo et al., 2015). A combined observational and modeling approach would provide a comprehensive characterization of the coastal circulation and benefit from the complementary nature of both systems. HF radar observations improve the model description by resolving low scale processes in areas with significant topographic gradients, whereas model outputs provide a 3-D qualitative picture with vertical resolution that completes the surface radar-derived information when the quality data or the spatiotemporal coverage are poorer.

This integrated strategy might complement and optimize the intense monitoring activity performed around the deltaic coastline through the timely and seamless delivery of high-quality operational products, devoted to support wise decision-making and mitigate anthropogenic hazards in the marine environment. Such products could also

OSD
12, 1913–1952, 2015

provide paramount information on biological connectivity between Ebro Delta marine protected area and other relevant ecological regions in the western Mediterranean Sea.

Acknowledgements. The authors gratefully acknowledge Qualitas Remos Company (partner of CODAR Ocean Sensors) for their useful suggestions. The Spanish Ministerio de Economía y Competitividad supported this study through the OPErational RAdars for research in marine sciences (OPERA) project (CTM2012-33223).

References

Alfonso, M., Álvarez-Fanjul, E., and López, J. D.: Comparison of CODAR SeaSonde HF Radar operational waves and currents measurements with Puertos del Estado buoys, Final Internal Report of Puertos del Estado, Madrid, Spain, 1–32, 2006.

Atwater, D. P. and Heron, M. L.: HF radar two-station baseline bisector comparisons of radial components, in: Proceedings of IEEE Oceans 2010, Sydney, Australia, 24–27 May 2010, 1–4, 2010.

Atwater, D. P. and Heron, M. L.: A first approach to SeaSonde quality control, in: Proceedings of IEEE Oceans 2011, Waikoloa, HI, USA, 1–5, 19–22 September, 2011.

Barrick, D. E. and Lipa, B. J.: Correcting for distorted antenna patterns in CODAR ocean surface measurements, IEEE J. Oceanic Eng., 11, 304–309, 1986.

Barrick, D. E., Fernandez, V., Ferrer, M. I., Whelan, C., and Breivik, Ø.: A short-term predictive system for surface currents from a rapidly deployed coastal HF radar network, Ocean Dynam., 62, 725–740, 2012.

Chapman, R. D. and Graber, H. C.: Validation of HF radar measurements, Oceanography, 10, 76–79, 1997.

Chapman, R. D., Shay, L. K., Graber, H. C., Edson, J. B., Karachintsev, A., Trump, C. L., and Ross, D. B.: On the accuracy of HF radar surface current measurements: intercomparison with ship-based sensors, J. Geophys. Res., 102, 18737–18748, 1997.

Codar Ocean Sensors: SeaSonde Diagnostic Files, CODAR Internal Document, California, USA, May, 2005.

Cosoli, S., Mazzoldi, A., and Gacic, M.: Validation of surface current measurements in the Northern Adriatic Sea from high frequency radars, J. Atmos. Ocean. Tech., 27, 908–919, 2010.

OSD

12, 1913–1952, 2015

Cosoli, S., Gacic, M., and Mazzoldi, A.: Surface current variability and wind influence in the north eastern Adriatic Sea as observed from high-frequency (HF) radar measurements, Cont. Shelf Res., 33, 1–13, 2012a.
Cosoli, S., Bolzon, G., and Mazzoldi, A.: A real-time and offline quality control methodology for SeaSonde high-frequency radar currents, J. Atmos. Ocean. Tech., 29, 1313–1328, 2012b.
Cosoli, S., Licer, M., Vodopivec, M., and Malacic, V.: Surface circulation in the Gulf of Trieste (northern Adriatic Sea) from radar, model, and ADCP comparisons, J. Geophys. Res., 118, 6183–6200, 2013.
Crombie, D. D.: Doppler spectrum of sea echo at 13.56 Mc/s, Nature, 175, 681–682, 1955.
De Paolo, T. and Terrill, E. J.: Skill assessment of resolving ocean surface current structure using compact-antenna-style HF radar and the MUSIC direction-finding algorithm, J. Atmos. Ocean. Tech., 24, 1277–1300, 2007.
De Paolo, T., Terril, E., and Kirincich, A.: Improving SeaSonde radial velocity accuracy and variance using radial metrics, IEEE Oceans 2015, Genova, Italy, 18–21 May 2015, 1–9, 2015.
Emery, B. and Washburn, L.: Evaluation of SeaSonde Hardware Diagnostic Parameters as Performance Metrics, NOAA IOOS final report, California USA, 2007.
Emery, B., Washburn, M. L., and Harlan, J. A.: Evaluating radial current measurements from CODAR high frequency radars with moored current meters, J. Atmos. Ocean. Tech., 21, 1259–1271, 2004.
Emery, W. J. and Thomson, R. E.: Data Analysis Methods in Physical Oceanography, Elsevier Science, Amsterdam, 2001.
Espino, M., Sanchez-Arcilla, A., and Garcia, M. A.: Wind induced mesoscale circulation off the Ebro Delta, NW Mediterranean: a numerical study, J. Marine Syst., 16, 235–251, 1998.
Font, J.: A comparison of seasonal winds with currents on the continental slope of the Catalan sea (Northwestern Mediterranean), J. Geophys. Res., 95, 1537–1545, 1990.
Font, J., Salat, J., and Tintore, J.: Permanent features of the circulation in the Catalan Sea, Oceanol. Acta, 9, 51–57, 1988a.
Font, J., Salat, J., and Wang, D. P.: Lagrangian and Eulerian observation of inertial oscillations in the shelf break offshore the Ebro River Delta (Catalan Sea, NW Mediterranean), Rapp. Comm. Int. Mer Médit, 31, 2, 1988b.

OSD
12, 1913–1952, 2015

Font, J., Garcia-Ladona, E., and Gorriz, E. G.: The seasonality of mesoscale motion in the Northern Current of the Western Mediterranean: several years of evidence, Oceanol. Acta, 18, 207–219, 1995.

Garcia, M. A. and Ballester, A.: Notas acerca de la meteorología y la circulación local en la región del Delta del Ebro, Invest. Pesq., 48, 469–493, 1984.

Gomez, R., Helzel, T., Petersen, L., Kniephoff, K., Merz, C. R., Liu, Y., and Weisberg, R. H.: Real-time quality control of current velocity data on individual grid cells in WERA HF radar, Oceans 2014, Taipei, Taiwan, 7–10 April 2014, 1–7, 2014.

Gomez, R., Helzel, T., Merz, C. R., Liu, Y., Weisberg, R. H., and Thomas, N.: Improvements in ocean surface radar applications through real-time data quality-control, Conference: Current, Waves and Turbulence Measurement (CWTM), IEEE/OES, Florida, USA, 2–6 March 2015, 1–9, 2015.

Gonella, J.: A rotary-component method for analyzing meteorological and oceanographic vector time series, Deep Sea Res. Pt. II, 19, 833–846, 1972.

Graber, H. C., Haus, B. K., Shay, L. K., and Chapman, R. D.: HF radar comparisons with moored estimates of current speed and direction: expected differences and implications, J. Geophys. Res., 102, 749–766, 1997.

Jimenez, J. A., Guillen, J., Sanchez-Arcilla, A., Gracia, V., and Palanques, A.: Influence of benthic boundary layer dynamics on wind-induced currents in the Ebro Delta inner shelf, J. Geophys. Res., 107, 1–10, 2002.

Kaplan, D. M. and Lekien, F.: Spatial interpolation and filtering of surface current data based on open-boundary modal analysis, J. Geophys. Res.-Oceans, 112, C12007, doi:10.1029/2006JC003984, 2007.

Kaplan, D. M., Largier, J., and Botsford, L. W.: HF radar observations of surface circulation off Bodega Bay (northern California, USA), J. Geophys. Res., 110, 1–25, 2005.

Kaihatu, J. M., Handler, R. A., Marmorino, G. O., and Shay, L. K.: Empirical orthogonal function analysis of ocean surface currents using complex and real-vector methods, J. Atmos. Ocean. Tech., 15, 927–941, 1998.

Kirincich, A. R., de Paolo, T., and Terrill, E.: Improving HF radar estimates of surface currents using signal quality metrics, with application to the MVCO High-Resolution Radar System, J. Atmos. Ocean. Tech., 29, 1377–1390, 2012.

Kohut, J. T. and Glenn, S. M.: Improving HF radar surface current measurements with measured antenna beam patterns, J. Atmos. Ocean. Tech., 20, 1303–1316, 2003.

OSD
12, 1913–1952, 2015

Kovačević, V., Gačić, M., Mancero Mosquera, I., Mazzoldi, A., and Marinetti, S.: HF radar observations in the northern Adriatic: surface current field in front of the Venetian Lagoon, J. Marine Syst., 51, 95–122, 2004.
Kundu, P.: Ekman veering observed near the ocean bottom, J. Phys. Oceanogr., 6, 238–242, 1976.
Kundu, P. K. and Allen, J. S.: Some three-dimensional characteristics of low-frequency current fluctuations near the Oregon coast, J. Phys. Oceanogr., 6, 181–199, 1976.
Levanon, N.: Lowest GDOP in 2-D scenarios, IEE P.-Radar Son. Nav., 147, 149–155, 2000.
Lipa, B., Nyden, B., Ullman, D. S., and Terrill, E.: SeaSonde radial velocities: derivation and internal consistency, IEEE J. Oceanic Eng., 31, 850–861, 2006.
Liu, Y., Weisberg, R. H., and Merz, C. R.: Assessment of CODAR SeaSonde and WERA HF Radars in mapping surface currents on the West Florida Shelf, J. Atmos. Ocean. Tech., 31, 1363–1382, 2014.
Lorente, P., Piedracoba, S., Soto-Navarro, J., and Alvarez-Fanjul, E.: Accuracy assessment of high frequency radar current measurements in the Strait of Gibraltar, J. Operational Oceanography, 7, 59–73, 2014.
Lorente, P., Piedracoba, S., Soto-Navarro, J., Ruiz, M. I., Alvarez-Fanjul, E., and Montero, P.: Towards the implementation of a fully operational HF coastal radar network operated by Puertos del Estado, IEEE Oceans 2015, Genova, Italy, 18–21 May 2015, 1–6, 2015a.
Lorente, P., Piedracoba, S., and Alvarez-Fanjul, E.: Validation of high-frequency radar ocean surface current observations in the NW of the Iberian Peninsula, Cont. Shelf Res., 92, 1–15, 2015b.
Lorente, P., Piedracoba, S., Soto-Navarro, J., and Alvarez-Fanjul, E.: A combined QC methodology in Ebro Delta HF radar system: real time web monitoring of diagnostic parameters and offline validation of current data, European Geosciences Union General Assembly (EGU), Vienna, Austria, 12–17 April 2015, 17, EGU2015-11440, 2015c.
Ohlmann, C., White, P., Washburn, L., Terril, E., Emery, B., and Otero, M.: Interpretation of coastal HF radar-derived currents with high-resolution drifter data, J. Atmos. Ocean. Tech., 24, 666–680, 2007.
Paduan, J. D., Kim, K. C., Cook, M. S., and Chavez, F. P.: Calibration and validation of direction-finding High-Frequency radar ocean surface current observations, IEEE J. Oceanic Eng., 31, 862–875, 2006.

OSD
12, 1913–1952, 2015

Robinson, A. M., Wyatt, L. R., and Howarth, M. J.: A two year comparison between HF radar and ADCP current measurements in Liverpool Bay, J. Operational Oceanography, 4, 33–45, 2011.
Salat, J., Garcia, M. A., Cruzado, A., Palanques, A., Arín, L., Gomis, D., Guillen, J., de León, A., Puigdefàbregas, J., Sospedra, J., and Velásquez, Z. R.: Seasonal changes of water mass structure and shelf-slope exchanges at the Ebro Shelf (NW Mediterranean), Cont. Shelf Res., 22, 327–348, 2002.
Roarty, H., Smith, M., Kerfoot, J., Kohut, J., and Glenn, S.: Automated Quality Control of High Frequency Radar Data, IEEE Oceans 2012, Hampton Roads, Virginia, VA, USA, 14–19 October 2012, 1–7, doi:10.1109/OCEANS.2012.6404809, 2012.
Rypina, I. I., Kirincich, A. R., Limeburner, R., and Udovydchenkov, I. A.: Eulerian and Lagrangian correspondence of high-frequency radar and surface drifter data: effects of radar resolution and flow components, J. Atmos. Ocean. Tech., 31, 945–966, 2014.
Schmidt, R.: Multiple emitter location and signal parameter estimation, IEEE T. Antenn. Propag., 34, 276–280, 1986.
Shay, L. K., Cook, T. M., Peters, H., Mariano, A. J., Weisberg, R., Edgar An, P., Soloviev, A., and Luther, M.: Very high-frequency radar mapping of surface currents, IEEE J. Oceanic Eng., 27, 155–169, doi:10.1109/JOE.2002.1002470, 2002.
Sotillo, M. G., Cailleau, S., Lorente, P., Levier, B., Aznar, R., Reffray, G., Amo-Baladrón, A., and Alvarez-Fanjul, E.: The MyOcean IBI Ocean Forecast and Reanalysis Systems: operational products and roadmap to the future Copernicus Service, J. Operational Oceanography, 1–18, 2015.
Taylor, K. E.: Summarizing multiple aspects of model performance in a single diagram, J. Geophys. Res., 106, 7183–7192, 2001.
Trujillo, D. A., Kelly, F. J., Perez, J. C., Riddles, H. R., and Bonner, J. S.: Accuracy of surface current velocity measurements obtained from HF radar in Corpus Christi Bay, Texas, Int. Geosci. Remote Se., 2, 1179–1182, 2004.
Wyatt, L.: Improving the quality control and accuracy of HF radar currents, IEEE Oceans 2015, Genova, Italy, 18–21 May 2015, 1–9, 2015.
Yoshikawa, Y., Masuda, A., Marubayashi, K., Ishibashi, M., and Okuno, A.: On the accuracy of HF radar measurement in the Tsushima strait, J. Geophys. Res., 111, C04009, doi:10.1029/2005JC003232, 2006.

OSD
12, 1913–1952, 2015

Table 1. Diagnose parameters used to operationally monitor Ebro Delta HF radar status in real time. The HF radar system's performance is routinely evaluated through the analysis of the belowlisted indicators on different frequencies (daily/weekly/monthly).

SITE STATUS		
Type	Parameter	Description
Receiver	MTMP, RTMP	Chassis and board temperatures.
Transmitter	XPHT, XAHT	Chassis and amplifier temperatures.
Transmitter	XAFW, XARW	Forward and reflected powers.
Antenna	SNR1, SNR2, SNR3	Signal-to-Noise ratio at loop 1, loop 2 and the monopole.
Antenna	AMP1, AMP2	Calculated amplitude corrections for loops 1 and 2 to the monopole.
Radial	Number radials/u.t, Range and bearing	Abrupt decrease can be related to a potential malfunction
SYSTEM STATUS		
Parameter		Description
Temporal coverage		Data availability (%): areas of poor data return (< 50 %) are discarded from any analysis.
Evolution of spatial coverage		Monitoring of fluctuations due to day/night cycle. Identification of time-steps of sharp decrease in spatial coverage.
Spatial coverage–VS–Temporal coverage		Verification of the 80–80 % recommended level of data provision.
COS uncertainty metrics (standard deviation of U/V, covariance U/V)		Useful resource, based on fluctuations in the data themselves.

OSD
12, 1913–1952, 2015

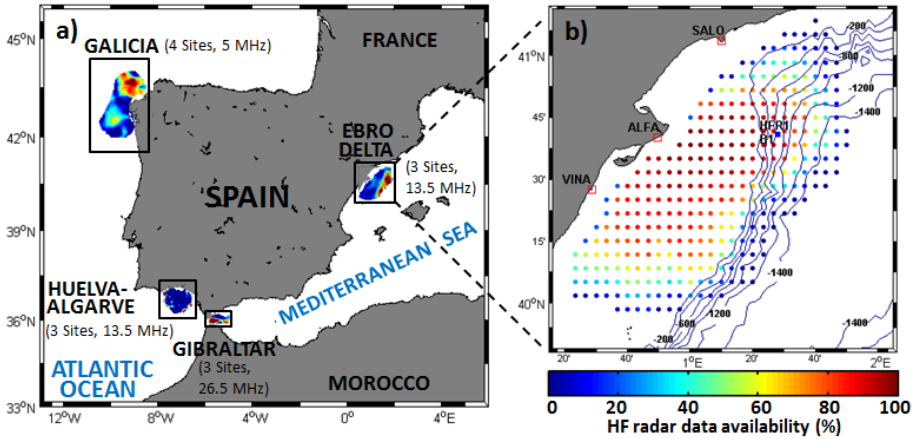

Figure 1. (a) HF coastal radar network currently operated by Puertos del Estado **(b)** HF radar deployed at the Ebro Delta, composed by three sites: Salou (SALO), Alfacada (ALFA) and Vinaroz (VINA). Colored dots denote the temporal coverage in percent of HF radar surface current total vectors for the entire year 2014. Isobath depths are labeled every 200 m. Location of Tarragona buoy (B1) is marked with filled blue squares. HFR1 denotes the radar grid point closest to B1 position.

OSD
12, 1913–1952, 2015

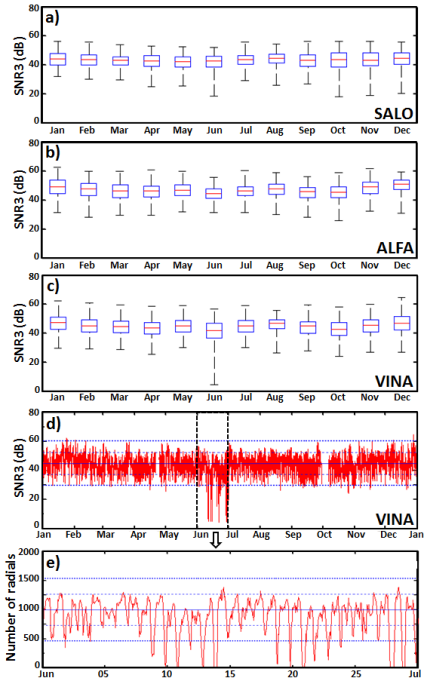

Figure 2. Annual quality control of Ebro Delta radar sites, SALO **(a)**, ALFA **(b)** and VINA **(c)**, based on monthly boxplots of Signal-to-Noise Ratio at the monopole (SNR3) for 2014. On each box, the central mark is the median, the edges of the box are the 25th and 75th percentiles, and the whiskers extend to the most extreme data points. An abrupt decrease (below 10 dB) is observed in VINA in June. The annual time serie of hourly SNR3 values for VINA site **(d)** reveals that the imposed thresholds of two standard deviations above/below the mean (bold blue dotted lines) are exceeded several times along June, reaching extremely low values which are related to a lower number of radial vectors provided by VINA site **(e)**. The solid and dashed blue lines represent the mean and the standard deviation for the entire 2014, respectively.

OSD
12, 1913–1952, 2015

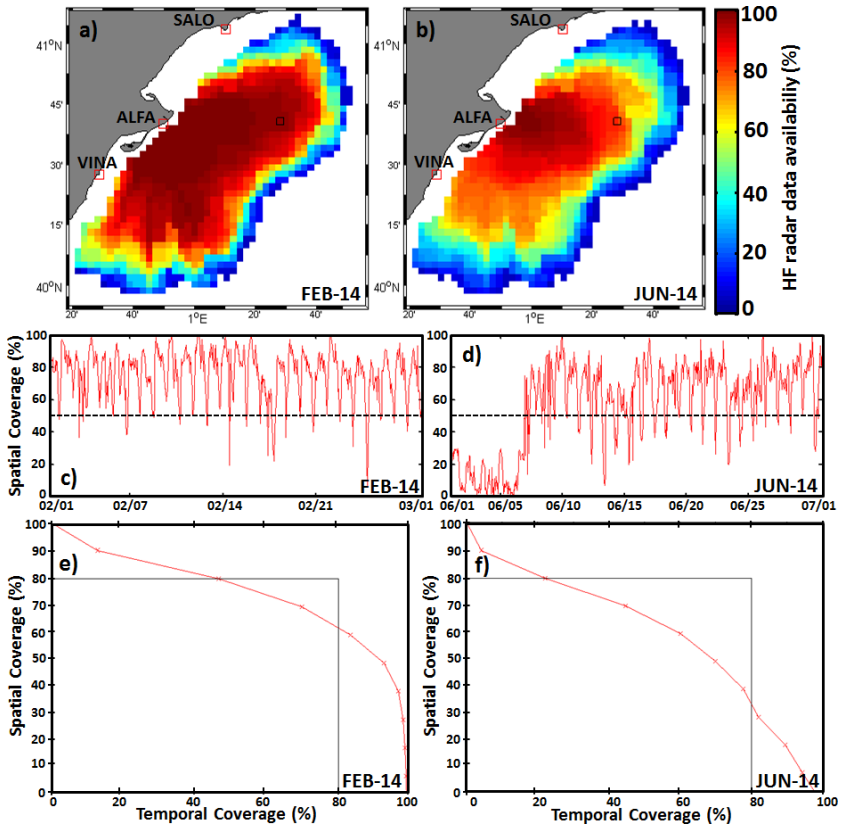

Figure 3. Evaluation of Ebro Delta HF radar system performance on a monthly basis: February (left) and June (right), 2014. A comparative analysis is carried out for the radar data availability (**a** and **b**), the temporal evolution of the spatial coverage (**c** and **d**) and the relationship between both the spatial and temporal coverage (**e** and **f**). The black square represented in (**a** and **b**) denotes B1 buoy location.

OSD
12, 1913–1952, 2015

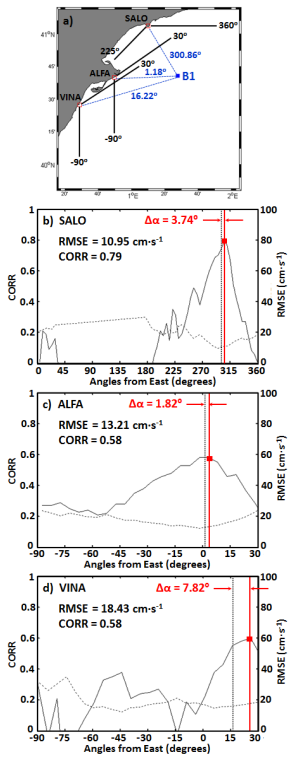

Figure 4. (a) Angular position of Ebro Delta HF radar sites respect to B1 buoy location. Angle values are measured counter-clockwise from East, indicating arc limits and buoy direction. **(b–d)** Correlation (solid line) and RMSE (dashed line) between unfiltered radial currents estimated by B1 buoy and those measured by three HF radar sites, SALO **(b)**, ALFA **(c)**, and VINA **(d)**, using calibrated antenna patterns for a 6 month period May–October 2014. Vertical dotted line represents the angular position of B1. Vertical red solid line denotes the angular position of maximum correlation (CORR), which is gathered with the associated RMSE and bearing offset ($\Delta\alpha$) values.

OSD
12, 1913–1952, 2015

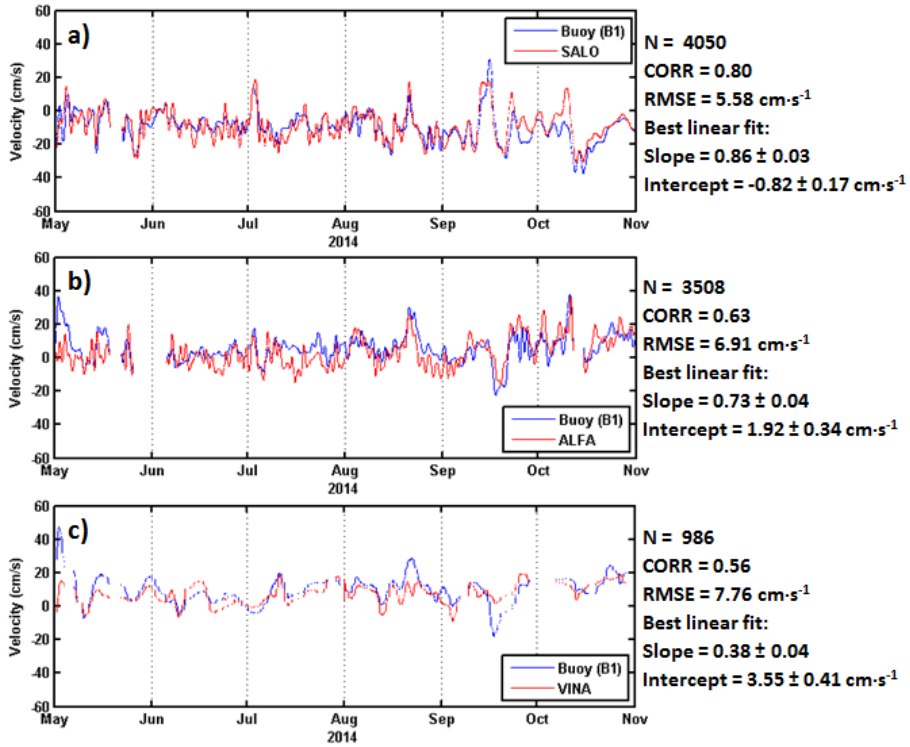

Figure 5. Comparison of low-pass filtered hourly time series (cut-off period of 30 h) of radial currents measured by B1 buoy (blue line) and HF radar sites (red lines): **(a)** SALO, **(b)** ALFA and **(c)** VINA in the range arc point closest to B1 location for a 6 month period May–October 2014, using calibrated antenna patterns. *N*, slope and intercept represent the number of hourly radial current observations and the results derived from the best linear fits, respectively.

OSD
12, 1913–1952, 2015

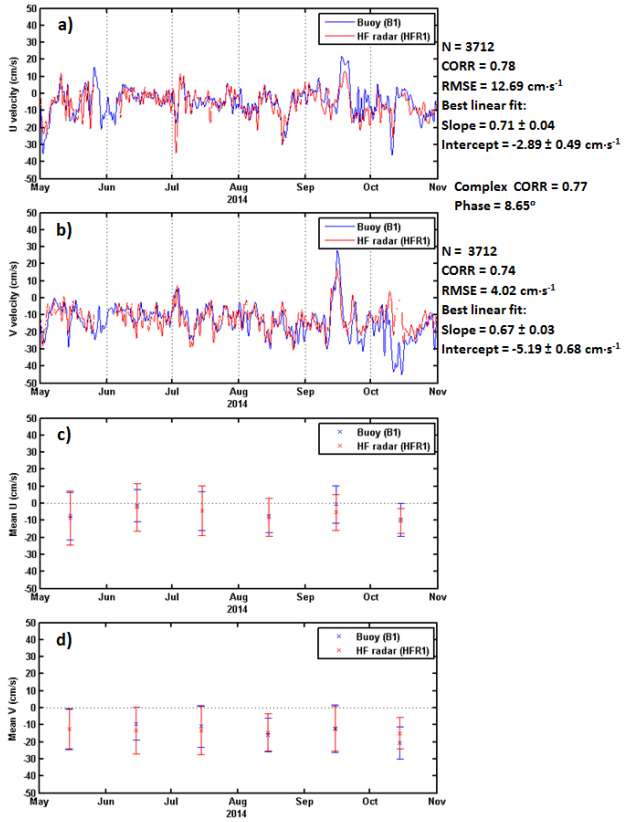

Figure 6. Low-pass filtered (cut-off period of 30 h) hourly time series of zonal **(a)** and meridional **(b)** components of total currents measured by B1 buoy (blue line) and HF radar at the closest grid point HFR1 (red line), for a 6 month period May–October 2014. Mean zonal **(c)** and meridional **(d)** current velocities, averaged over individual months for both HF radar and B1 measurements, with one standard deviation (error bars represent the 95 % confidence interval).

OSD
12, 1913–1952, 2015

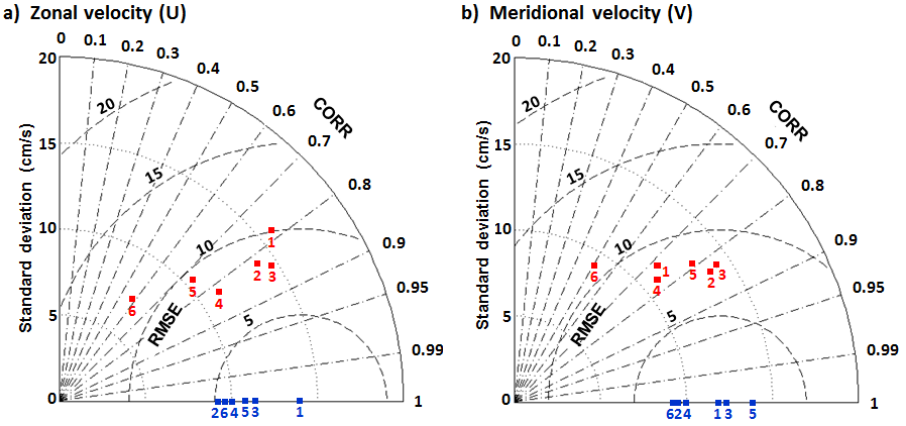

Figure 7. Taylor diagrams, based on the law of cosines, provide a concise statistical summary of how closely unfiltered hourly radar estimations (red filled squares) match with B1 observations (blue filled squares), considered here as the reference points of perfect agreement. Taylor diagrams for zonal **(a)** and meridional **(b)** velocity components gather the monthly statistical metrics derived from HF radar – B1 comparison. Sequential numbers refer to individual months of the analyzed period May–October 2014 (1: May; 6: October).

OSD
12, 1913–1952, 2015

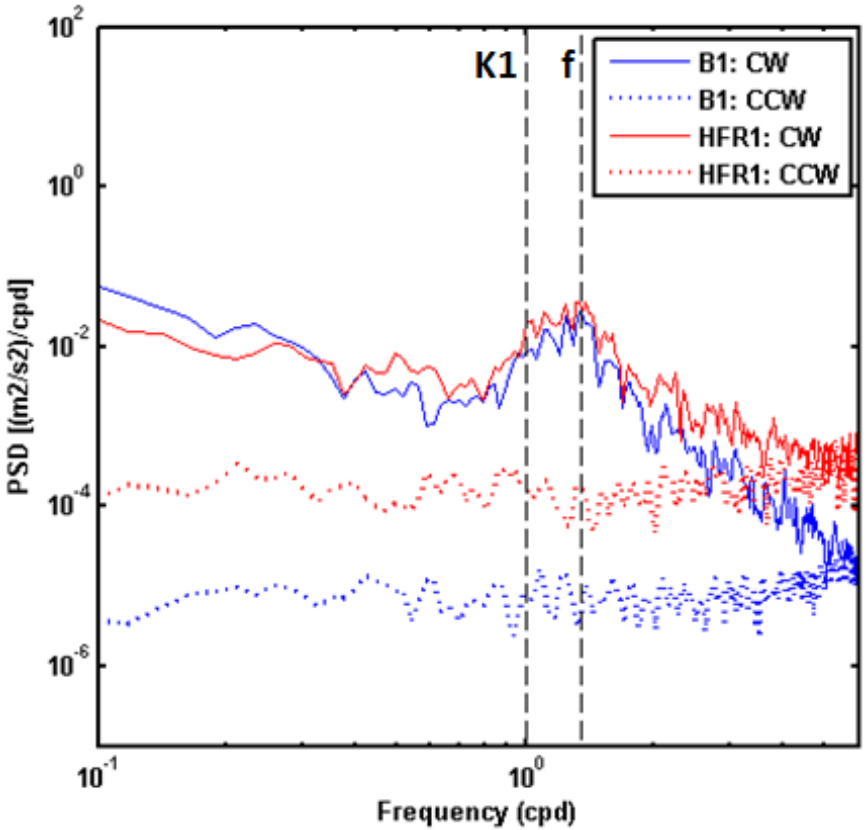

Figure 8. Spectral density of the rotary auto-spectra of B1 buoy (blue) and HF radar at the closest grid point HFR1 (red), performed for a 6 month period May–October 2014 of concurrent records. Clockwise (counter-clockwise) components are represented by solid (dotted) lines. Vertical dashed lines indicate the frequencies of the diurnal constituent (K_1) and the inertial oscillations (f).

OSD
12, 1913–1952, 2015

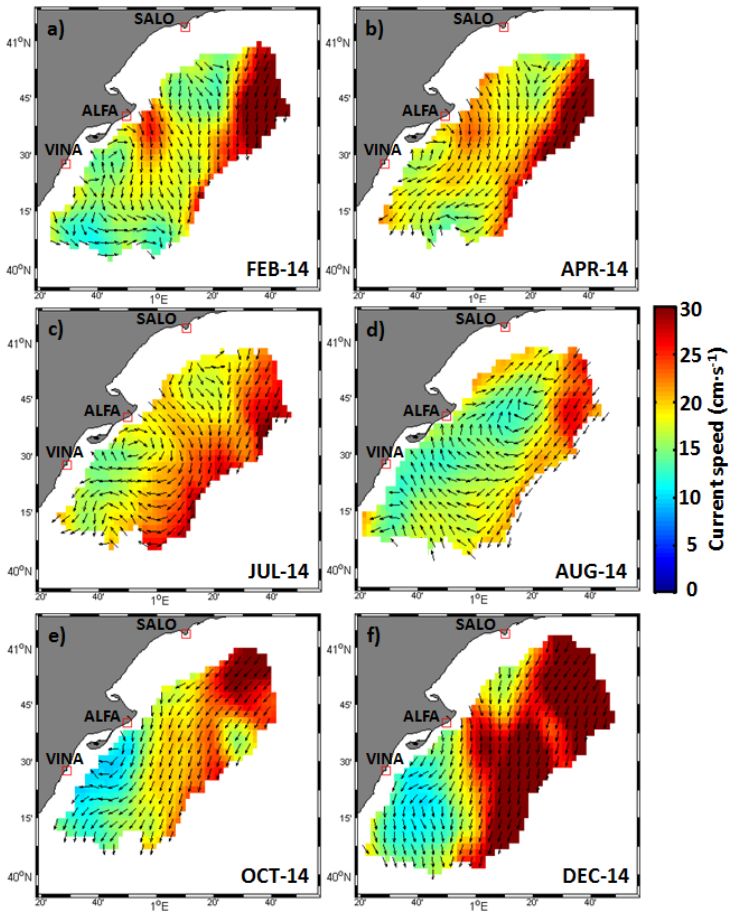

Figure 9. Monthly averaged surface velocity fields, based on unfiltered hourly HF radar current data, for **(a)** February, **(b)** April, **(c)** July, **(d)** August, **(e)** October, and **(f)** December 2014. Only one grid point of every two is plotted for visualization reasons.

OSD
12, 1913–1952, 2015

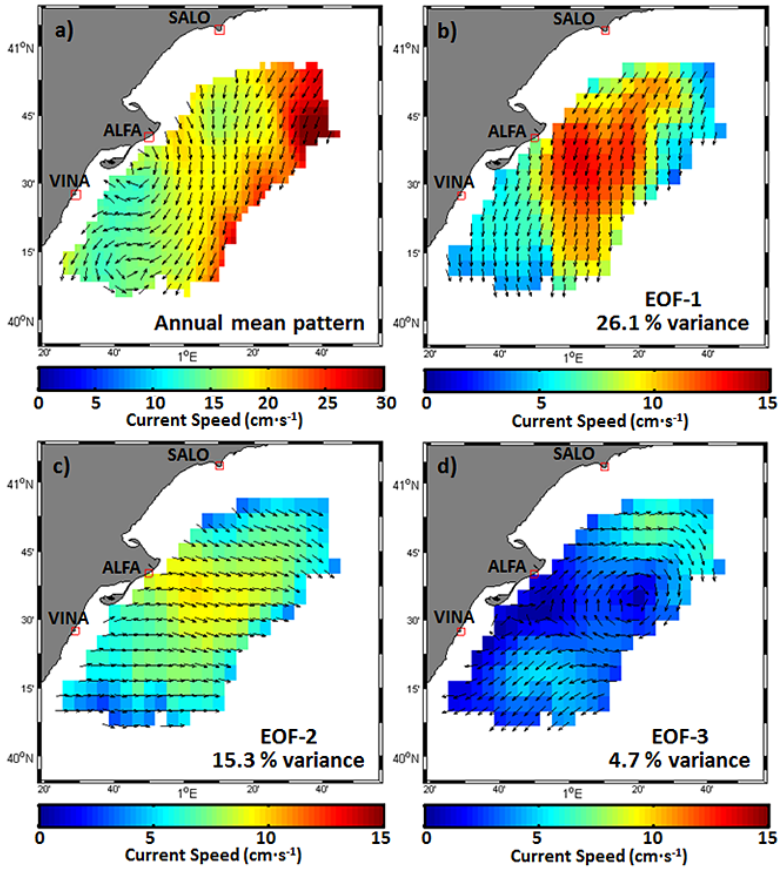

Figure 10. Spatial patterns of the **(a)** annual mean velocity field and **(b)** first, **(c)** second and **(d)** third EOF dominant modes of unfiltered hourly radar surface currents for 2014. Current vectors were plotted in every second grid point for clarity. Variance explained is indicated in the lower right corner of the corresponding panel.

OSD
12, 1913–1952, 2015

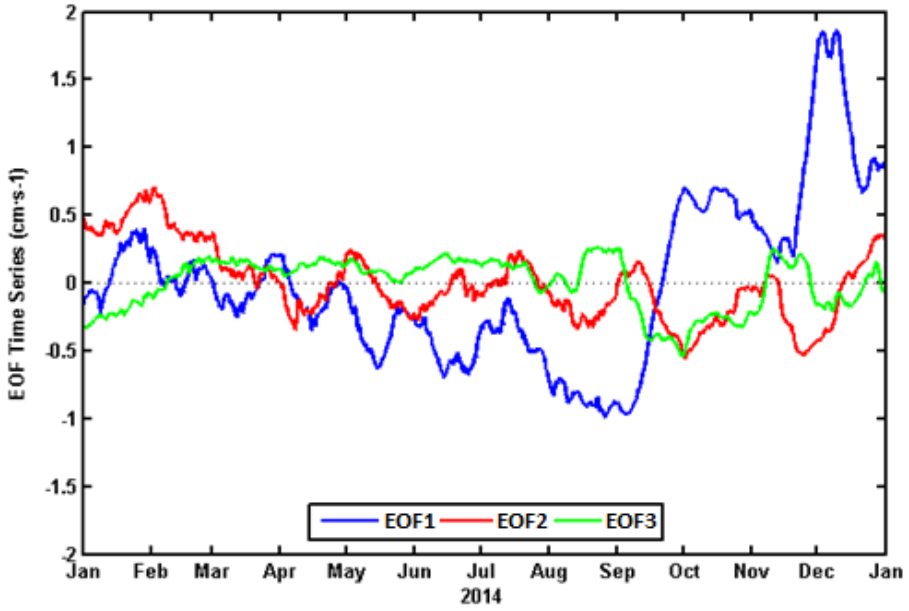

Figure 11. Time coefficients of the first (blue), second (red) and third (green) EOF modes of hourly radar current data set evaluated for the entire year 2014. Time series have been filtered with a 20 day running mean.

OSD
12, 1913–1952, 2015